JOURNAL OF EXPERIMENTAL AND THEORETICAL PHYSICS, 2024, Vol. 165, No. 4, pp. 533–541

SOLIDS AND LIQUIDS

ELECTRONIC STRUCTURE AND JAHN–TELLER DISTORTIONS IN FULLERENE COMPLEX $C_{60}^{\bullet-}$-MDABCO$^+$-TPC-I

© 2024 A. V. Kuzmin[a,*], S. S. Khasanov[a], D. V. Konarev[b]

[a] Institute of Solid State Physics named after Yu. A. Osipyan, Russian Academy of Sciences, 142432, Chernogolovka, Moscow region, Russia

[b] Federal Research Center for Chemical Physics and Medical Chemistry of the Russian Academy of Sciences, 142432, Chernogolovka, Moscow region, Russia

*e-mail: kuzminav@issp.ac.ru

Received October 30, 2023
Revised November 28, 2023
Accepted November 28, 2023

Abstract. Using X-ray diffraction analysis and quantum-chemical modeling methods, a crystal of a layered organic conductor based on fullerene radical anions, $C_{60}^{\bullet-}$-MDABCO+-TPC-I, has been studied. The quasi-two-dimensional electronic structure of its conducting fullerene layers, types of monoanion deformation and their causes from the perspective of Jahn–Teller interactions have been investigated. It has been shown that crystallographically nonequivalent fullerenes are characterized by different cage distortions, which result in significant differences in the electronic band diagrams of the corresponding fullerene layers.

Keywords: *organic conductors, crystal structure, low temperatures, fullerenes, quantum mechanical calculations, band structure*

DOI: 10.31857/S004445102404e072

1. INTRODUCTION

Polyaromatic anions with high symmetry can serve as a basis for the synthesis of materials with unusual chemical and physical properties [1]. For example, according to theoretical modeling, the ground state of dianions can be triplet, which is promising for design of molecular magnets [2]. One of such polyaromatic anions are the reduced forms of C_{60}^{n-} fullerenes. Obtaining ionic fullerene C_{60} compounds in crystalline form made it possible to study the structure and properties of such highly symmetric molecules and complexes based on them experimentally. For example, M_3C_{60} crystalline salts (M – metal) with C_{60}^{3-} trianions have cubic symmetry and possess metallic conductivity. Moreover, in these compounds transition to a superconducting state is observed at temperatures of 17–33 K [3]. Neutral C_{60} has high I_h symmetry and a triply degenerate lowest unoccupied molecular orbital (LUMO). When forming C_{60}^{n-} anions in a complex ionic compound, the LUMO orbital of fullerene is populated with additional n electrons. There may be cases when it becomes energetically favorable for the anion to deform own cage in a certain way, lowering its symmetry, and thereby removing the degeneracy in its electronic. Such interactions are called Jahn–Teller effects. They are often observed in solutions with ions of highly symmetric molecules, however, they can also occur in crystalline forms of ionic compounds, including fullerene ones [4].

Of particular interest are layered radical anion C_{60} salts with hexagonal or trigonal crystal symmetry. Crystals of such compounds exhibit metallic properties over a wide temperature range and unusual magnetic states with strong spin frustration due to the triangular arrangement of $C_{60}^{\bullet-}$ [5–10]. This work examines in detail the molecular and electronic band structure of the fullerene anionic complex $C_{60}^{\bullet-}$-MDABCO$^+$-TPC-I with $C_{60}^{\bullet-}$ triangular sublattice. A unique feature of the complex is that besides fullerene, it contains only C_3-symmetric molecules: the cation MDABCO$^+$ – N-methyldiazabicyclooctane and TPC-I – triptycene-iodide. The use of highly symmetric counterions and spacer molecules allowed preserving the high symmetry of fullerene layers, thus opening the possibility for formation of non-trivial collective electron states in them. The complex is isostructural to the previously studied crystal $C_{60}^{\bullet-}$-MDABCO$^+$-TPC-H [10], except for the replacement of one apical hydrogen in the

triptycene molecule with an iodine atom. It was shown that in the case of $C_{60}^{\bullet-}$-MDABCO$^+$-TPC-H, the fullerene layers have metallic conductivity at liquid nitrogen temperatures, become dielectric at helium temperatures, and at high temperatures undergo an order-disorder phase transition with loss of conductivity in one of the layers [10]. One of the hypothetical reasons for the peculiarities of low-temperature behavior of the complex may be non-trivial Jahn–Teller interactions that arise in the sublattices of $C_{60}^{\bullet-}$ radical anions. However, at that time, the quality of single-crystal structural data for $C_{60}^{\bullet-}$-MDABCO$^+$-TPC-H was not sufficient to reliably estimate the $C_{60}^{\bullet-}$ cage distortion parameters in the temperature ranges of interest and take into account their contribution to the electronic band structure of the crystals. In the new complex $C_{60}^{\bullet-}$-MDABCO$^+$-TPC-I with modified triptycene, reliable structural data was obtained with inconsistence factors $R_1 < 5\%$. Based on the new data, we conducted a comparative analysis of geometric distortions of the $C_{60}^{\bullet-}$ cages and results of quantum-chemical calculations of the electronic spectra of functional fullerene layers.

2. EXPERIMENTAL SECTION

Crystals $C_{60}^{\bullet-}$-MDABCO$^+$-TPC-I were prepared following the previously described synthesis conditions [10]. Structural data were obtained at 120 K using Mo K_α-radiation using a laboratory RigakuOxford Diffraction GeminiR CCD diffractometer with a four-circle k goniometer in a full sphere of scattering vector limitation $q = 4\pi\sin\theta / \lambda = 8.377$ Å^{-1}, which allowed subsequent analysis of the structure in a low-symmetry approximation. The electronic structure of $C_{60}^{\bullet-}$ anions was calculated using the Extended Hückel Method (EHM) using the YAeHMOP software package [11] with a basisv of atomic s-, p-orbitals of Slater type, STO-SZ for C, H, N atoms and STO-DZ for iodine I atoms [12]. The input parameters used were atomic coordinates obtained from X-ray diffraction analysis without preliminary geometry optimization. The parameters of Slater functions were taken as optimized as a result of fitting to density functional theory calculations for a series of similar compounds [13]. For calculations of band structure, density of states and potential energy surface, a combined method was used – EHM + tight-binding method with an unbiased mesh of special k-points with density 11×11×11, constructed according to the Monkhorst-Pack scheme [14].

3. RESULTS AND DISCUSSION

3.1. Crystal Structure of $C_{60}^{\bullet-}$-MDABCO$^+$-TPC-I

At room temperature, the $C_{60}^{\bullet-}$-MDABCO$^+$-TPC-I complex crystallizes in the trigonal symmetry group $R\bar{3}$ (the symmetry of the fullerene position in the crystal is C_{3v}) [10]. In the first approximation, this trigonal symmetry is preserved at low temperatures. To exclude the influence of the overall high symmetry when analyzing the molecular structure of fullerene and its cage distortions, the refinement of the crystal structure as a whole was

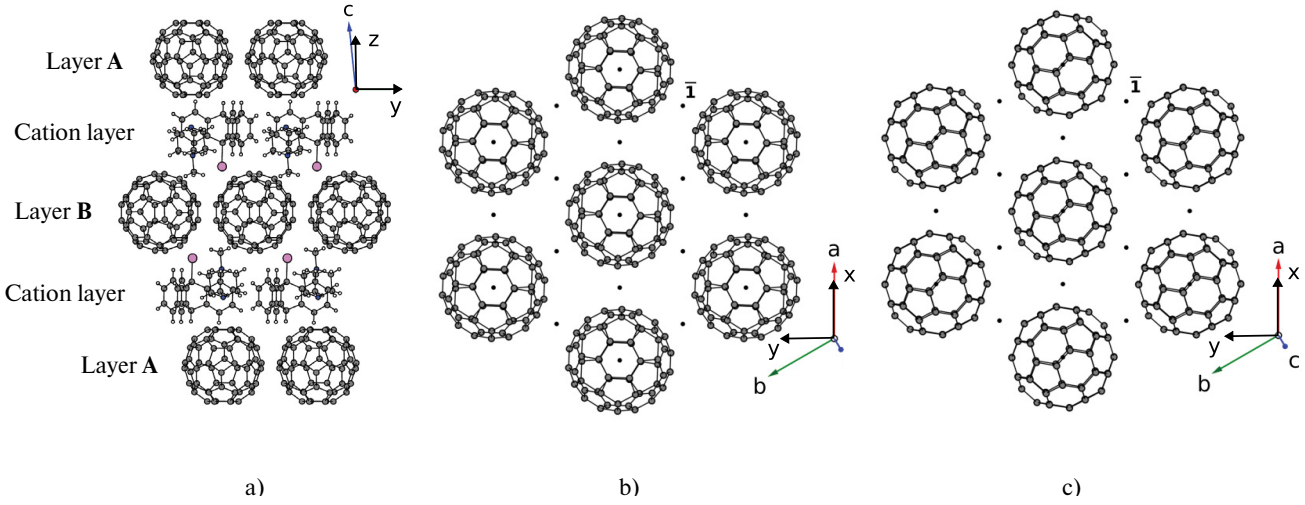

Fig. 1. a) Layered structure of $C_{60}^{\bullet-}$-MDABCO$^+$-TPC-I crystals; b) view of layer A along direction c*; c) view of layer B along direction c*; *a, b, c* are directions of crystallographic coordinate axes, x, y, z are Cartesian coordinate system corresponding to crystallographic one

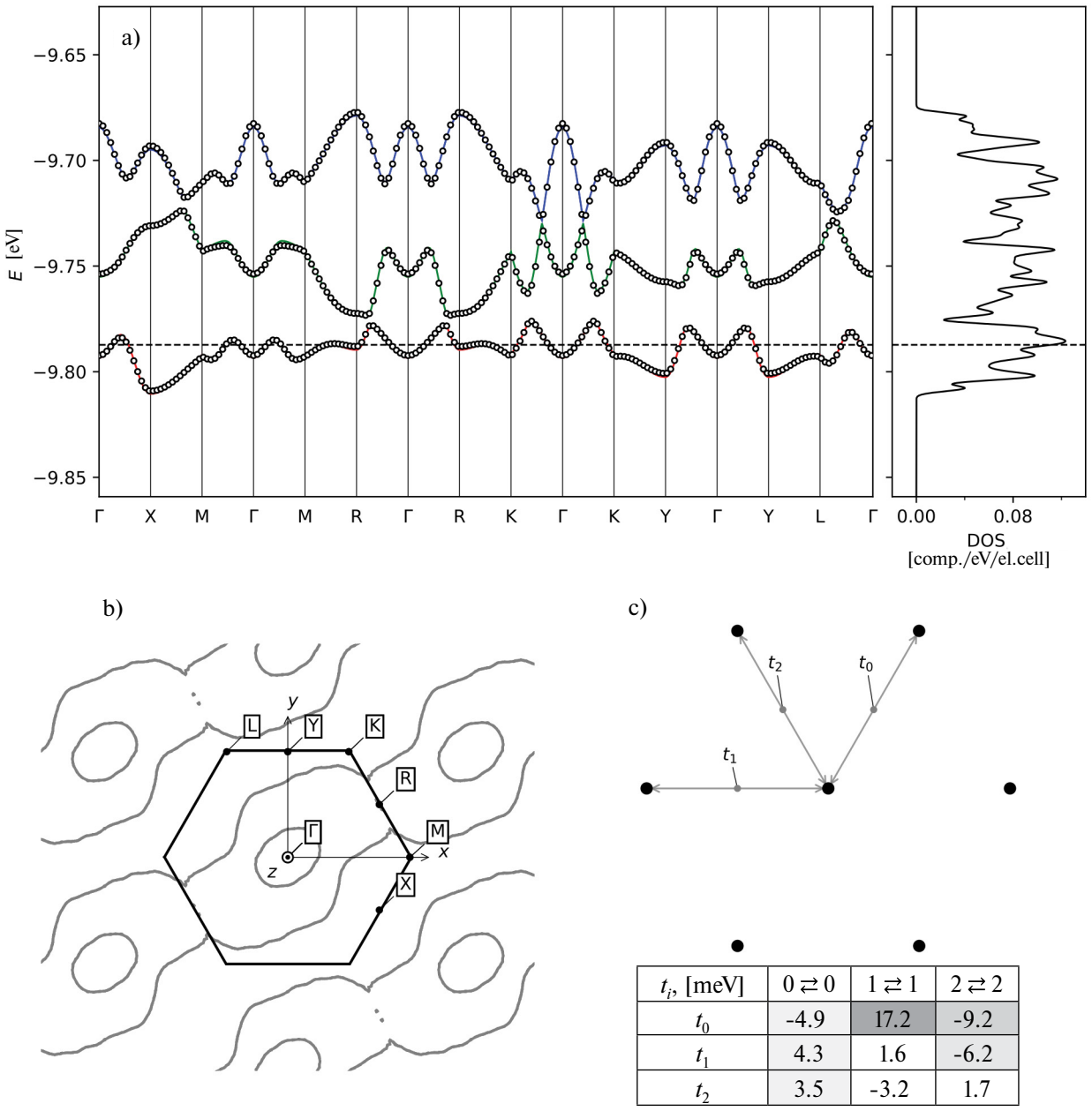

t_i, [meV]	0 ⇄ 0	1 ⇄ 1	2 ⇄ 2
t_0	-4.9	17.2	-9.2
t_1	4.3	1.6	-6.2
t_2	3.5	-3.2	1.7

Fig. 2. Band structure, density of states (a), Fermi surface (b), and transfer integrals t_i (c) for the layer **A** of crystal $C_{60}^{\bullet-}$-MDABCO$^+$-TPC-I

carried out in triclinic setting in the symmetry approximation $P\bar{1}$. When the temperature drops below 200 K, weak lattice distortions are observed, leading to a reduction in the symmetry of the fullerene position to C_i. At temperature $T = 120$ K the lattice parameters are a = 9.956(1) Å, b = 9.961(1) Å, c = 28.437(3) Å, α = 90.23(1)°, β = 99.65(1)°, γ = 119.95(1)°, V = 2396.8(1) Å^3, which corresponds to the primitive cell of the initial trigonal lattice. The choice of such setting is due to the fact that in this case, the axes a and b lie in the plane of fullerene close-packed layers. The complex structure is similar to the previously described structure [10] and represents a layered packing of $C_{60}^{\bullet-}$ anionic fullerene and cationic MDABCO$^+$-TPC-I layers (see Fig. 1 b, c). The difference in layers lies in the mutual orientation of fullerenes in the layer and their cationic environment. Type **A** fullerenes are packed in such a way that locally in the anionic layer the third-order axis is preserved, and the MDABCO$^+$ and TPC-I cations point their apical substituents in opposite directions relative to the

layer plane. Type **B** fullerenes are oriented with their double C = C bond toward the cationic layer, and the methyl group $MDABCO^+$ and I point inside the interstitial space of the fullerene layer sublattice.

3.2. Electronic structure of fullerene layers

For band structure calculations of layers **A** and **B**, the coordinates of atoms of the target layer and two cation layers surrounding this fullerene layer were used as input parameters. This approach allows taking into account the electrostatic influence of cations and most correctly assessing the charge distribution in $C_{60}^{\bullet-}$.

Figs. 2 and 3 show the results of band structure calculations for layers **A** and **B**. The points in Fig. 2a and Fig. 3a show the dispersion curves obtained by the EHM method and passing through symmetric points of the Brillouin zone: Γ = (0,0,0), X = (1 / 2,0,0), M = (2 / 3,1 / 3,0), R = (1 / 2,1 / 2,0), K = (1 / 3,2 / 3,0), Y = (0,1 / 2,0), L = (–1 / 3,1 / 3,0). Figs. 2b and 3b contain cross-sections of the Fermi surface in the layer plane.

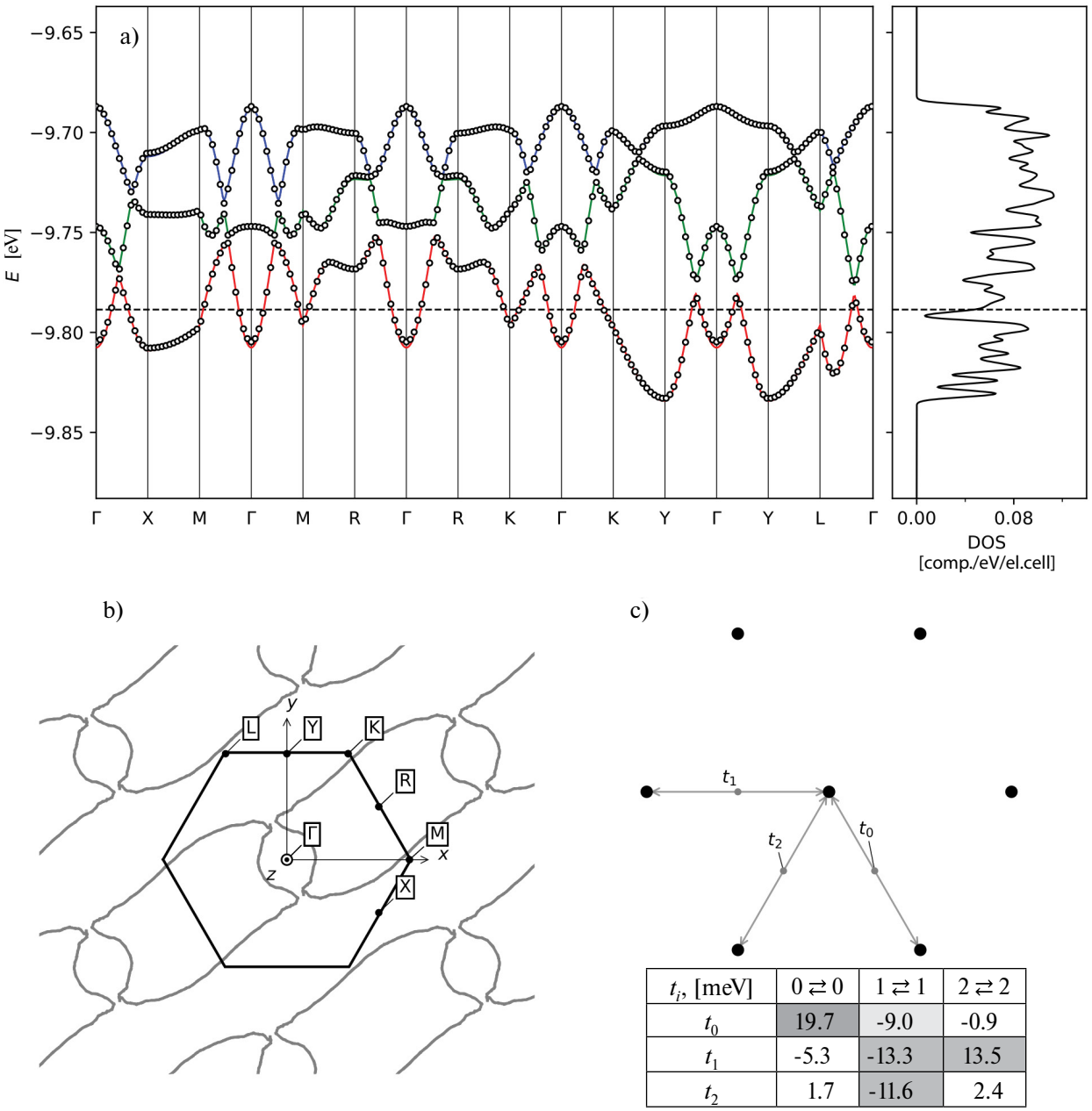

t_i, [meV]	0 ⇄ 0	1 ⇄ 1	2 ⇄ 2
t_0	19.7	-9.0	-0.9
t_1	-5.3	-13.3	13.5
t_2	1.7	-11.6	2.4

Fig. 3. Band structure, density of states (a), Fermi surface (b), and transfer integrals t_i (c) for the layer **B** of crystal $C_{60}^{\bullet-}$-$MDABCO^+$-TPC-I

Primary analysis of band diagrams shows that layer **A** is characterized by relatively narrow bands – 33 meV, 50 meV and 52 meV, the lowest, narrowest of them, is partially filled. The density of states at the Fermi level is relatively high and equals 0.112 eV^{-1} per unit cell. The narrowness of the band indicates weak electronic interaction between nodes of the triangular sublattice $C_{60}^{\bullet-}$.

In layer **B**, conversely, there is significant curvature of the lower band through which the Fermi level passes (see Fig. 3). This is especially noticeable in directions Γ-K-Y, which determines the fairly large widths of the lower conduction band and two upper valence subbands (81 meV, 64 meV and 48 meV). The density of states at the Fermi level for layer **B** is almost twice lower than that for layer **A** and amounts to 0.047 eV^{-1} per unit cell.

Solid lines in the band diagrams (Figs. 2a and Fig. 3a show the results of fitting dispersion curves obtained from EHM with curves $E(k)$ obtained by the tight-binding method, where three fullerene orbitals serve as the basis ϕ_0^{LUMO}, ϕ_1^{LUMO}, ϕ_2^{LUMO}. It can be seen that the tight-binding method describes the calculated EHM curves well. In neutral fullerene, they are the lowest unoccupied molecular orbitals (LUMO) and are triply degenerate due to the icosahedral symmetry of the C_{60} cage. In the anion $C_{60}^{\bullet-}$ one of the LUMO levels is populated by an additional electron, however, to maintain analogy, the same orbital names will be used. In such a basis, the one-electron wave function in a periodic potential will represent a Bloch sum

$$\psi_k(r) \propto \sum_{n=0}^{2} c_n(k) \sum_{\tau} e^{i(k\cdot\tau)} \phi_i^{\mathrm{LUMO}}(r-\tau)$$

over basis functions n and nearest neighbors τ. The transfer integrals between LUMO obtained in this way:

$$t_\tau(i \rightleftarrows j) = \int (\phi_i^{\mathrm{LUMO}}(r))^* \widehat{H} \phi_i^{\mathrm{LUMO}}(r-\tau)dr,$$

where

$$\widehat{H} = -\frac{\hbar^2}{2m}\nabla^2 + U(r)$$

is the electron Hamiltonian in periodic potential $U(r)$, are shown in Fig. 2c.

It can be seen that the values $|\, t_\tau(0 \rightleftarrows j)\,|$ between the lowest energy orbitals ϕ_0^{LUMO} do not exceed 5 meV and are close to each other in magnitude. This indicates that electrons on the frontier orbitals $C_{60}^{\bullet-}$ interact weakly with each other, therefore the electronic subsystem of fullerene layer **A** is more similar to a system of weakly interacting spins $S = 1/2$ in a triangular sublattice.

The energy structure of the three molecular orbitals of layer **A** can be estimated by the value

$$e_{ii} = \int (\phi_i^{\mathrm{LUMO}}(r)) \cdot \widehat{H} \phi_i^{\mathrm{LUMO}}(r)dr.$$

Fig. 4 shows the values e_{ii} for three levels ϕ_i^{LUMO} and zone energies at point Γ. As shown by the level diagram e_{ii}, in each type of anions, three LUMO levels are split according to the scheme 2+1, where the electron-occupied level is lowered in energy relative to others: $e_{00} = -9.7724$ eV, $e_{11} = -9.7439$ eV, $e_{22} = -9.7249$ eV for layer **A** and $e_{00} = -9.7801$ eV, $e_{11} = -9.7360$ eV, $e_{22} = -9.7219$ eV for layer **B**. This degeneracy scheme is typical for monoanions $C_{60}^{\bullet-}$ [15].

3.3. Deformations in $C_{60}^{\bullet-}$ cage

Comparing the electronic structures of layers **A** and **B** (particularly, the functionally significant lowest half-filled subband), one can conclude that they significantly differ from each other. The reasons for such differences may lie in non-trivial distortions of basic anion $C_{60}^{\bullet-}$ cage, which have a Jahn–Teller nature. It is known that the energy correction to the intra-site energy (on the fullerene anion) associated with Jahn–Teller distortions can cause a change

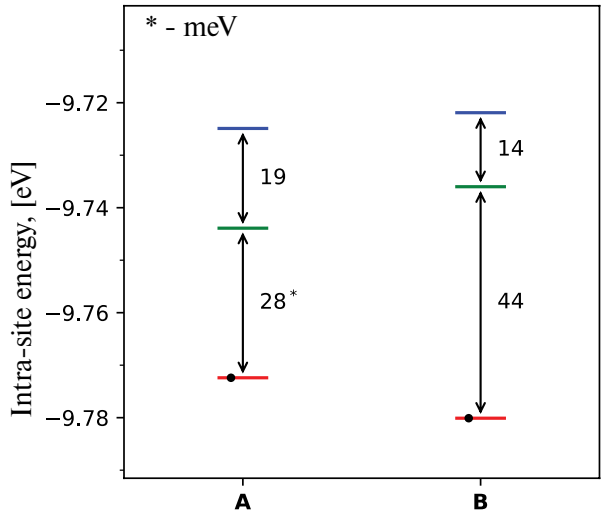

Fig. 4. Energy values e_{ii} of three LUMO levels of **A** and **B** type anions in crystal $C_{60}^{\bullet-}$-MDABCO$^+$-TPC-I, the lower occupied level of anion is marked with a dot

in intersite electronic interactions throughout the layer [16].

To characterize distortions in fullerene anions, including Jahn–Teller ones, it is convenient to use the method of approximating its deformed cage with an ellipsoid.

The ellipsoid axis lengths ν_1, ν_2 and ν_3 obtained this way allow determining the main direction of distortions, and the difference in axis lengths can be a reliable estimate of deformation degree. Moreover, this approach allows describing the fine structure of deformations, for which one can use deformation maps constructed from atom deviations $C_{60}^{\bullet-}$ from the equivalent sphere surface.

The results of the deformation analysis of fullerene **A** cages are presented in Fig. 5. The average radius of the ionic fullerene cage is close to the radius of the neutral one C_{60} with optimized geometry [17] and equals 3.549 Å. The axis lengths of the approximating ellipsoid of the fullerene from layer **A** are $\nu_1 = 3.542$ Å, $\nu_2 = 3.546$ Å, $\nu_3 = 3.558$ Å. Thus, in the first approximation, the cage is described by a rotation ellipsoid. The longest axis of the layer **A** fullerene ellipsoid (the "distinguished" deformation axis), as axis ν_3, is oriented along the crystallographic direction [001] and perpendicular to the fullerene layer plane (a,b) (Fig. 5 c). Additionally, in the deformation structure of anion **A**, a narrow equatorial compression region

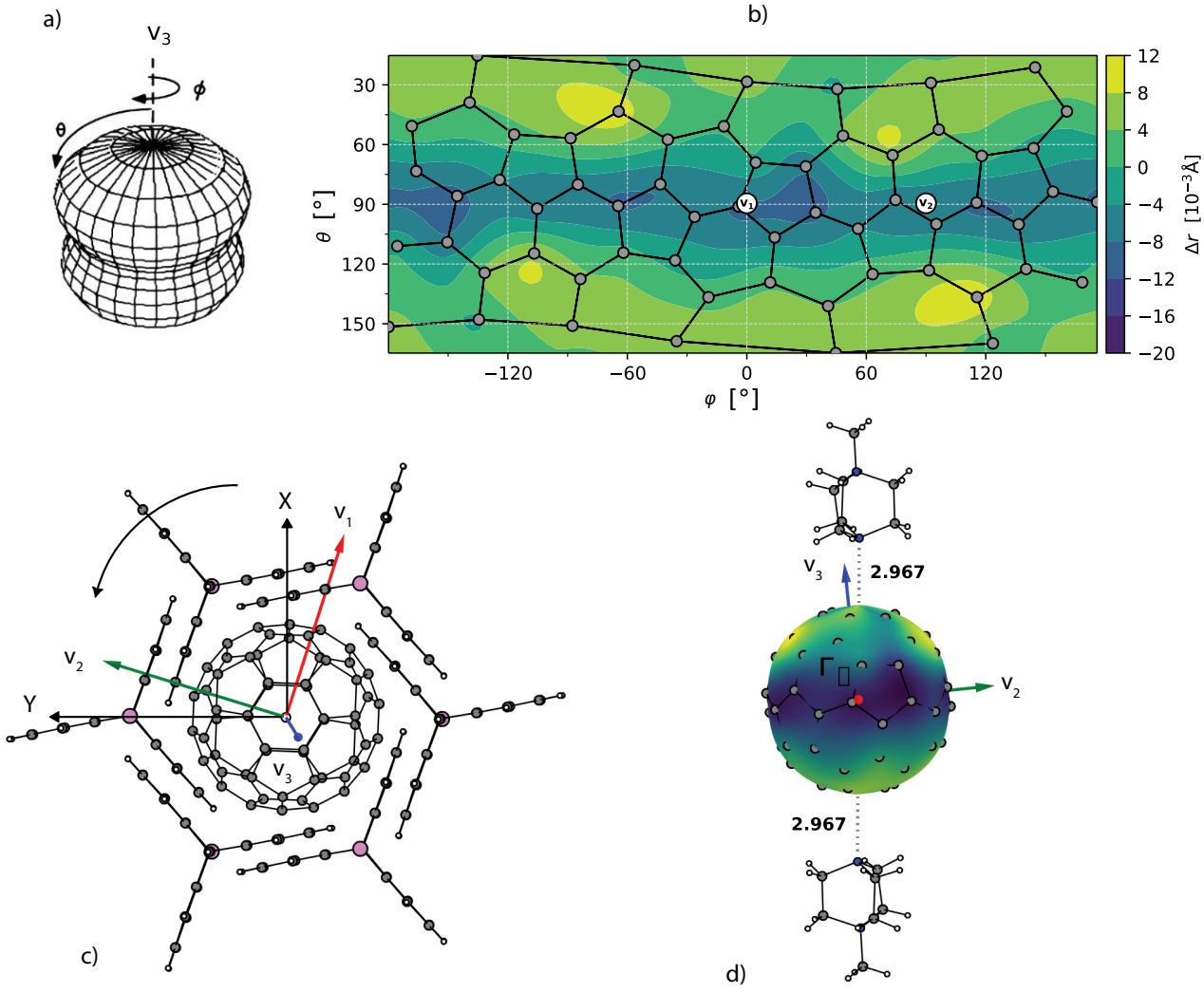

Fig. 5. Deformation structure in layer **A** anions: spherical coordinate system and theoretical form of single-mode deformations of the radical anions relative to the sphere [18] (a), deformation map of layer **A** fullerenes showing carbon atom displacements relative to the sphere surface Δr (b), packing of **A**-anions and cation layer molecules (c), $MDABCO^+\cdots C_{60}^{\bullet-}\cdots MDABCO^+$ chain (all distances are given in Å) (d); ν_1, ν_2 and ν_3 are directions of the approximating ellipsoid axes

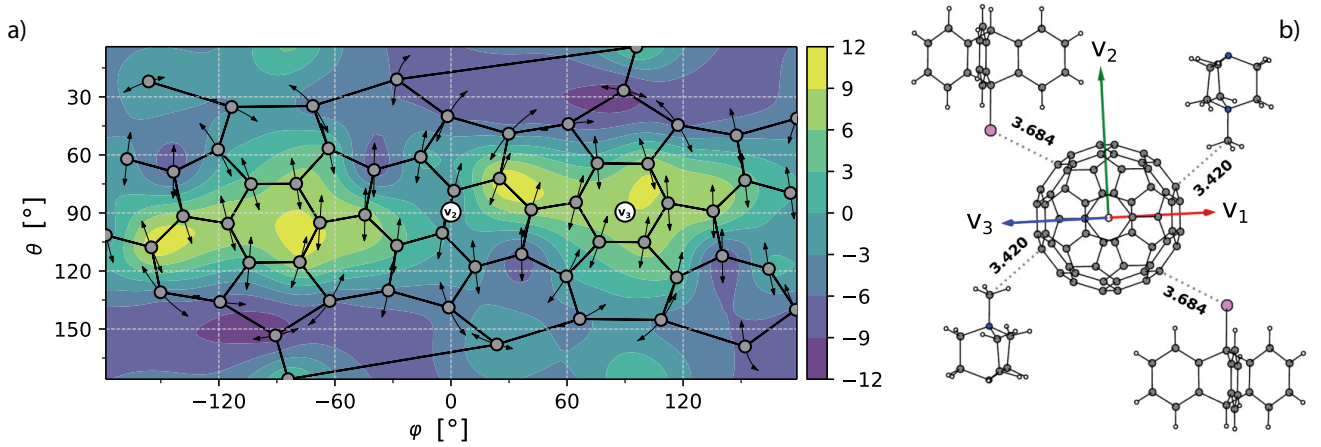

Fig. 6. Deformation map of layer **B** fullerenes, arrows show the maximum axes of ellipsoids of anisotropic carbon atom displacements (a), nearest environment of fullerene **B** in the crystal (all distances are given in) (b); ν_1, ν_2 and ν_3 are directions of the approximating ellipsoid axes

is distinguished (Fig. 5 b), the presence of which was theoretically predicted [18] (Fig. 5 a) and indicates a clear Jahn–Teller character of its cage distortion.

Typically, Jahn–Teller distortions of $C_{60}^{\bullet-}$ fullerene radicals have a relatively small magnitude in the series of anions C_{60}^{n-} [16] and are poorly recognized from single-crystal structural data, as they are often suppressed by external factors – crystal field, strong thermal vibrations, etc. However, in the case of layer anions **A** they have a pronounced character, which may be due to the unique position of the anion in the structure. Each anion of type **A** is located in cells formed by a network of TPC-I molecules (Fig. 5 c), with $MDABCO^+$ cations surrounding it from above and below (see Fig. 5d). In this case, the electrostatic field of the cations does not prevent but enhances uniaxial Jahn–Teller stretching deformations $C_{60}^{\bullet-}$. Such uniaxial deformations are not forbidden by layer symmetry (see Fig. 1b) and allow free rotation of the fullerene relative to the normal to the layer plane. However, in our case, the fullerene is rigidly fixed in its orientation both relative to the directions in the layer plane and normal to the layers.

To provide a complete picture of fullerene cage distortions, the following features should be noted. Structural analysis shows that carbon atoms of fullerene **A** are characterized by relatively small anisotropic displacement parameters, with atoms predominantly oscillating on the fullerene cage surface. The tangential axes of thermal ellipsoids

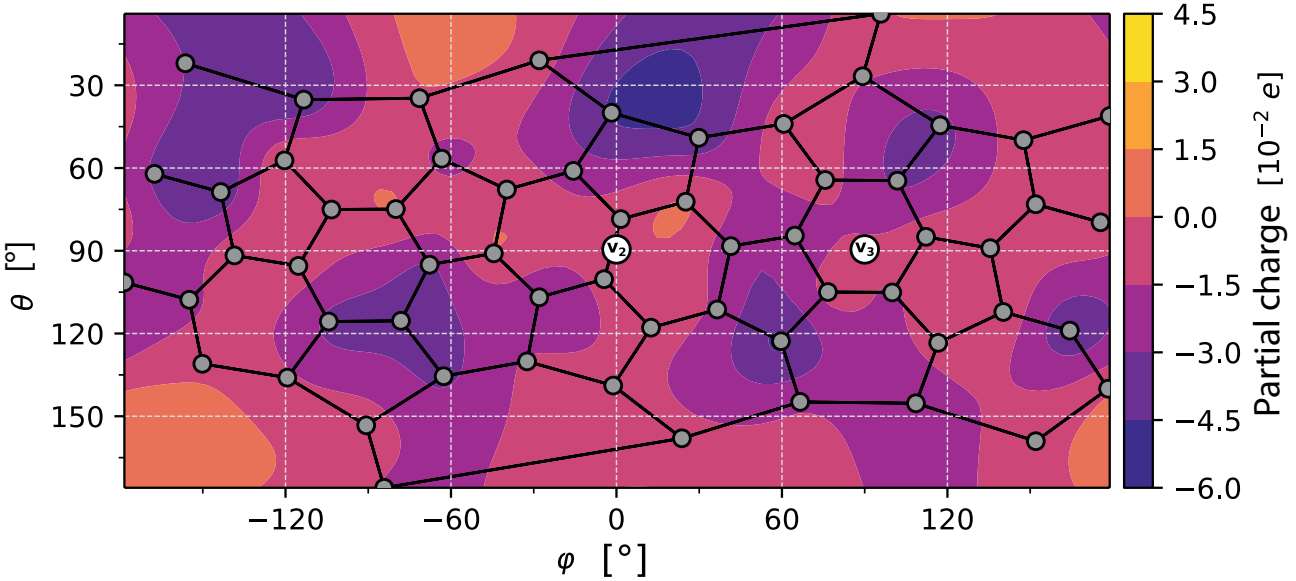

Fig. 7. Charge distribution map on the surface of fullerene layer **B**

(directions parallel to the surface) are twice as large as the radial component (directions along the radius): $U_{\parallel,1} = 0.163$ Å^2, $U_{\parallel,2} = 0.153$ Å^2, $U_{\perp} = 0.086$ Å^2. Essentially, the radial components of atomic displacements make a determining contribution to the distribution of deformed compression-tension areas of the fullerene cage, so their suppression may indicate a statically formed cage character and the absence of unaccounted "hidden" distortions of the fullerene anion.

The shape of fullerene layer **B** is of general form when compared to the fullerene from layer **A**. The average radius of the charged fullerene is 3.545 Å, and the axes lengths of the approximating ellipsoid are $\nu_1 = 3.538$ Å, $\nu_2 = 3.546$ Å and $\nu_3 = 3.552$ Å are equidistant from each other in length (differences between ellipsoid axis lengths are 0.008 Å and 0.006 Å).

On the deformation maps of the layer **B** fullerene cage (see Fig. 6 a), there are two symmetric convex regions near the ν_3 axis, which are not directly related to static Jahn–Teller interactions, as they are not described within the uniaxial deformation model (see Fig. 5 a). The complex shape of anion **B** and the presence of highly deformed regions near the ν_3 axis apparently results from the interaction of various factors: the crystal field effect formed by cationic layer components – electrostatic and steric influence of MDABCO$^+$ and iodine atoms (see Fig. 6 b), as well as intrinsic stresses in the anion cage in the form of Jahn–Teller interactions.

Regarding the first factor, i.e. the influence of MDABCO$^+$ cations as one of the causes of inhomogeneities in the deformed cage, it is evidenced by the uneven charge distribution on the anion (see Fig. 7). The surface charge map shows that the negative charge of fullerene **B** concentrates in isolated regions. These $C_{60}^{\bullet-}$ cage regions correspond to directions towards MDABCO$^+$ cations and TPC-I molecules from adjacent layers (see Fig. 6 b).

Considering the second factor, it should be noted that a situation is possible when Jahn–Teller distortions have a dynamic nature. Such deformations are extremely difficult to detect from structural data; however, dynamically distorted Jahn–Teller anions typically stand out from their crystalline environment due to an increased degree of structural disorder and are subject to strong librations due to the so-called pseudorotation. The consequence of cage pseudorotations may be that significant amplitudes of atomic vibrations are observed within the deformed regions. In this regard, it can be noted that the mean, equivalent to isotropic, square displacement of fullerene **B** carbons is noticeably higher than that of type **A** fullerene, and the atoms of anion **B**, as in the case of anion **A**, undergo strong displacements along the fullerene surface, however, the shape of their thermal ellipsoids is strongly elongated along one of the tangential directions: $U_{\parallel,1} = 0.236$ Å^2, $U_{\parallel,2} = 0.176$ Å^2, $U_{\perp} = 0.088$ Å^2 (see Fig. 6), indicating librational oscillations of the molecule.

4. CONCLUSION

In this work, based on the analysis of two crystallographically independent fullerene anions **A** and **B** in the compound $C_{60}^{\bullet-}$-MDABCO$^+$-TPC-I crystals, it was identified that uniaxial distortions of the first type anions have a Jahn–Teller nature, while the second type anions do not have a pronounced direction of distortions, although there are areas of significant deformations on their cages. The complicated corrugation of the **B** anions cages does not allow classifying these deformations as single-mode static Jahn–Teller distortions. The observed pattern of **B**-type anion cage distortions may be a consequence of multiple factors: fullerene pseudorotation due to the so-called dynamic Jahn–Teller effect, non-trivial crystal field effect, etc.

Another situation is observed with anions of type **A**, which are subject to the static Jahn–Teller effect. Uniaxial co-directed Jahn–Teller deformations $C_{60}^{\bullet-}$ in **A** impede interstitial conductivity in the fullerene sublattice and can lead to partial dielectrization of the layer. Indeed, analysis of the band structure of layer **A** shows that the anions are weakly bound to each other and will behave rather as an ensemble of isolated spins $S = 1/2$. This constitutes the difference in the behavior of crystals with modified ($C_{60}^{\bullet-}$-MDABCO$^+$-TPC-I and initial compositions. Crystals of the initial composition with unsubstituted triptycene $C_{60}^{\bullet-}$-MDABCO$^+$-TPC-H) demonstrated metallic character of the electron spectrum of the corresponding fullerene layer [10]. In general, antiferromagnetically interacting spins in the fullerene layers being localized would create prerequisites for non-trivial magnetic effects, in particular, it may lead to the formation of a collective spin liquid state in the frustrated triangular sublattice.

FUNDING

This work was supported by the Russian Science Foundation (project No. 22-23-01158).

REFERENCES

1. D.V. Konarev, R.N. Lyubovskaya, Molecular design, structure and properties investigation of fullerene ionic compounds, Russian Chemical Reviews 4, 336 (2012).
2. M. Baumgarten, in: EPR of Free Radicals in Solids II, Trends in Methods and Applications, Prog. T. Chem. (2012), p. 205.
3. M. J. Rosseinsky, Fullerene Intercalation Chemistry, J. Mater. Chem. 5, 1497 (1995).
4. D. V. Konarev, A.V. Kuzmin, S. V. Simonov et al., Experimental Observation of C_{60} LUMO Splitting in the C_{60}^{2-} Dianions Due to the Jahn–Teller Effect. Comparison with the $C_{60}^{\bullet-}$ Radical Anions, Phys. Chem. Chem. Phys. 15, 9136 (2013).
5. D. V. Konarev, S. S Khasanov, A. Otsuka et al., Metallic and Mott Insulating Spin- Frustrated Antiferromagnetic States in Ionic Fullerene Complexes with a Two- Dimensional Hexagonal $C_{60}^{\bullet-}$ Packing Motif, Chem. European. J. 20, 7268 (2014).
6. D. V. Konarev, S. S. Khasanov, Y. Shimizu et al., Fullerene and Endometallofullerene Kagome Lattices with Symmetry-Forced Spin Frustration, Phys. Chem. Chem. Phys. 21, 1645 (2018).
7. D. V. Konarev, S. S. Khasanov, H. Yamochi, and A. Otsuka, Synthesis, Structure, and Properties of the Fullerene C_{60} Salt of Crystal Violet, $(CV^{+})(C_{60}^{\bullet-}) \cdot 0.5C_6H_4Cl_2$, which Contained Closely Packed Zigzagged $C_{60}^{\bullet-}$ Chains, Chem. Asian J. 11, 1705 (2016).
8. D. V. Konarev, S. S. Khasanov, A. V. Kuzmin et al., Effective Magnetic Coupling with Strong Spin Frustration in $(Ph_3MeP^{+})(C_{60}^{\bullet-})$ and Reversible) $(C_{60}^{\bullet-})$ Dimerization in $(Ph_3MeP^{+}) \cdot (C_{60}^{\bullet-}) \cdot C_6H_5CN$. Effect of Solvent on Structure and Properties, New J. Chem. 40, 2792 (2016).
9. A. Otsuka, D. Konarev, R. Lyubovskaya et al., Design of Spin-Frustrated Monomer- Type $C_{60}^{\bullet-}$ Mott Insulator, Crystals. 8, 115 (2018).
10. D. V. Konarev, S. S Khasanov, A. Otsuka et al., A Two-Dimensional Organic Metal Based on Fullerene, Angew. Chem. Int. Ed. 49, 4829 (2010).
11. G. Landrum, YAeHMOP 3.0 (2023).
12. J. C. Slater, Atomic Shielding Constants, Phys. Rev. 36, 57 (1930)
13. E. V. Lenthe and E. J. Baerends, Optimized Slater-Type Basis Sets for the Elements 1- 118, J. Comput. Chem. 24, 1142 (2003).
14. H. J. Monkhorst and J. D. Pack, Special Points for Brillouin-Zone Integrations, Phys. Rev. B. 13, 5188 (1976).
15. Fullerene-Based Materials: Structures and Properties, ed. by K. Prassides, Springer (2009).
16. O. Gunnarsson, Alkali-Doped Fullerides: Narrow-Band Solids with Unusual Properties, World Scientific Publishing Company (2004).
17. B. I. Dunlap and R. R. Zope, Efficient Quantum-Chemical Geometry Optimization and the Structure of Large Icosahedral Fullerenes, Chem. Phys. Lett. 422, 451 (2006).
18. A. Auerbach, N. Manini, and E. Tosatti, Electron-Vibron Interactions in Charged Fullerenes. I. Berry Phases, Phys. Rev. B 49, 12998 (1994).